Journal of Magnetic Resonance 254 (2015) 98–109

Contents lists available at ScienceDirect

Journal of Magnetic Resonance

journal homepage: www.elsevier.com/locate/jmr

Bottom-up study of the MRI positive contrast created by the Off-Resonance Saturation sequence

S. Delangre [a], Q.L. Vuong [a], D. Henrard [a], C. Po [b], B. Gallez [b], Y. Gossuin [a,*]

[a] Biomedical Physics Department, Université de Mons, Place du Parc 20, 7000 Mons, Belgium
[b] Biomedical Magnetic Resonance Research Group, Louvain Drug Research Institute, Université Catholique de Louvain, Brussels, Belgium

ARTICLE INFO

Article history:
Received 21 October 2014
Revised 12 February 2015
Available online 9 March 2015

Keywords:
Magnetic resonance imaging
Positive contrast imaging
Off-resonance imaging
Iron oxide nanoparticles
Superparamagnetic nanoparticles
Contrast agents

ABSTRACT

Superparamagnetic iron oxide nanoparticles (SPM particles) are used in MRI to highlight regions such as tumors through negative contrast. Unfortunately, sources as air bubbles or tissues interfaces also lead to negative contrast, which complicates the image interpretation. New MRI sequences creating positive contrast in the particle surrounding, such as the Off-Resonance Saturation sequence (ORS), have thus been developed. However, a theoretical study of the ORS sequence is still lacking, which hampers the optimization of this sequence. For this reason, this work provides a self-consistent analytical expression able to predict the dependence of the contrast on the sequence parameters and the SPM particles properties. This expression was validated by numerical simulations and experiments on agarose gel phantoms on a 11.7 T scanner system. It provides a fundamental understanding of the mechanisms leading to positive contrast, which could allow the improvement of the sequence for future *in vivo* applications. The influence of the SPM particle relaxivities, the SPM particle concentration, the echo time and the saturation pulse parameters on the contrast were investigated. The best contrast was achieved with SPM particles possessing the smallest transverse relaxivity, an optimal particle concentration and for low echo times.

1. Introduction

Magnetic resonance imaging (MRI) is a powerful non-invasive technique that provides images with an excellent intrinsic contrast [1,2], but contrast agents are sometimes needed to highlight regions of interest such as tumors [3,4]. Among these contrast agents, superparamagnetic iron oxide nanoparticles (SPM particles) are used because they decrease the MRI signal intensity in their surrounding [4–6]. They are thus essentially used as negative contrast agents in T_2 or T_2^*-weighted imaging.

The main advantages of SPM particles are their non-toxicity and their functionalizable surface, which is valuable for molecular and cellular imaging applications [7–13]. Nowadays, thanks to the numerous studies devoted to the optimization of synthesis protocols [14–17] and of their relaxation properties [18–20], SPM particles are used in applications such as MRI monitored magnetic hyperthermia [21], tumors targeting [22–24] and drug delivery followed by MRI [25,26]. Unfortunately, in T_2 or T_2^*-weighted images, SPM particles are often not distinguishable from other sources of MRI signal loss such as air bubbles or tissue interfaces. Their detection can also be difficult in regions with poor signal. To overcome these problems, a current challenge is the development of new imaging methods leading to positive contrast nearby SPM particles [27–30].

There are four categories of SPM particle positive contrast sequences. (1) The first category uses frequency selective pulses during/before the signal excitation as the "Off-Resonance Imaging" sequence [31–33] or the ON-Resonance Saturation method [34–38]. (2) The second category uses off-resonance effects during the signal formation and/or acquisition as the "white-marker" method [39–42] or the co-RASOR technique [43]. (3) Some techniques are based on post-processing image analysis as phase gradient imaging [44,45], susceptibility weighted imaging [46] or multiple off-resonance reconstructions of a single acquisition [47]. (4) At last, a sequence using Ultrashort Echo Time has been used [48,49].

In this work, we study the Off-Resonance Saturation (ORS) method [50–53]. This sequence, belonging to the first category, uses a preliminary off-resonance saturation pulse that spoils the signal created by water protons situated nearby the SPM particles. The positive contrast is then achieved by subtracting the resulting image from an image obtained without saturation pulse.

* Corresponding author at: Biomedical Physics Department, University of Mons, Avenue du champ de mars, 24, 7000 Mons, Belgium.
E-mail address: yves.gossuin@umons.ac.be (Y. Gossuin).

http://dx.doi.org/10.1016/j.jmr.2015.02.014
1090-7807/

An advantage of this method is its easy implementation on an MRI scanner, as it can be used with any conventional MRI sequence. Moreover, artifacts produced by magnetic inhomogeneities originating from the apparatus or the patient body can be distinguished from the SPM positive contrast by varying the saturation pulse parameters [40].

The efficiency of the ORS method has already been demonstrated *in vitro* and *in vivo* [50–53]. However, these studies did not determine an optimal set of sequence and particle parameters to use to achieve the best contrast. This is only possible if a full theoretical study is made on this sequence. In the long term, such a theoretical expression of the contrast could also help for the determination of the particle concentration *in vivo*, which is an important feature for applications as cellular and molecular imaging. To our knowledge, the only theoretical ORS sequence study was done in [53]. However, this model is only effective with a soft continuous saturation RF pulse, and is thus inapplicable with a short saturation pulse as used in our work.

In this article, we will provide a theoretical model of ORS able to predict the positive contrast in function of the sequence parameters and of the SPM particles properties. Our theory will allow the determination of the optimal sequence parameters and SPM particle properties in order to maximize the contrast. This can also enable the determination of the most suitable SPM particles for specific applications. Our theory will then be validated by both numerical simulations and MRI experiments on agarose gel phantoms with different types of SPM particles. The influence of the imaging sequence parameters as the echo time, the saturation pulse parameters, the particle concentration and relaxivity on the contrast will be experimentally investigated.

2. Theory

The theoretical model describing the ORS sequence developed in this work uses a bottom-up approach, starting from fundamental theoretical derivations of the Bloch equations [54,55] and finally providing an analytical expression of the contrast. The ORS sequence principle is first described. An analytical expression of the ORS contrast is then provided.

2.1. ORS principle

At high field, when the SPM magnetization interaction with the field is larger than the thermal energy, a SPM particle can be modeled as a magnetic dipole aligned with the external magnetic field $\vec{B}_0$ (aligned with the *z*-axis). This dipole creates a dipolar magnetic field (Fig. 1) whose component along the z axis (the *x* and *y* components can be neglected if $\vec{B}_0$ is large enough) is given by

$$B_{dip}(\vec{r}) = \frac{B_{eq}R_p^3}{r^3}(3\cos^2\theta - 1), \tag{1}$$

where R_p is the SPM particle radius, $\vec{r}$ is the vector connecting the center of the particle to the considered position, θ is the angle between $\vec{r}$ and $\vec{B}_0$ and B_{eq} its equatorial field of the SPM particle. This last quantity is the magnitude of the field created by the SPM particle at its equator, and is proportional to the particle magnetization M_S (expressed here as $Am^2/kg[Fe]$). For magnetite, which composes the SPM particles used in the present work, B_{eq} is given by [18,38]

$$B_{eq} = 0.72 \times 5185 \times \frac{\mu_0}{3} M_S \tag{2}$$

where 0.72 is the fraction of iron in magnetite, 5185 is the magnetite density (kg/m^3) and μ_0 is the magnetic permeability of the vacuum.

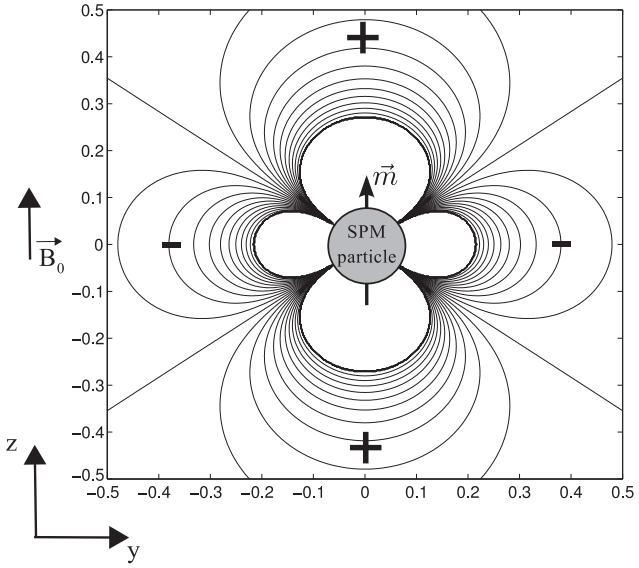

Fig. 1. Isofield lines of the dipolar magnetic field created by a SPM particle possessing a magnetic moment $\vec{m}$.

The dipolar magnetic field created by the SPM particles induces an angular frequency shift of the water proton at position $\vec{r}$ equal to

$$\omega_{dip} = \gamma B_{dip} \tag{3}$$

where γ is the proton gyromagnetic ratio. This implies a frequency distribution in a solution containing SPM particles calculated in [56] and presented on Fig. 2a.

The ORS (Off-Resonance Saturation) method consists in subtracting two MR images acquired with the same MR imaging sequence [52]. The first image is acquired with the chosen imaging sequence. The second one is acquired with the application of a frequency selective saturation pulse before the imaging sequence. Thanks to the dipolar field created by the SPM particles, the saturation pulse can be tuned to spoil (saturate) only the MRI signal created by the protons in the SPM particles vicinity, leaving the protons situated far enough from the SPM particles unspoiled (unsaturated) (Fig. 2b). In this way, the MR images obtained with and without the application of the saturation pulse present different MRI signal intensity only in regions containing SPM particles (Fig. 2c). Therefore, the ORS image obtained by the subtraction of these two images leads to positive contrast near SPM particles (Fig. 2c).

The saturation pulse parameters, i.e. its bandwidth $\Delta\omega$ and its frequency offset ω_0 (Fig. 2b), must be chosen in order to only spoil the water protons in the SPM particles vicinity. Therefore, these parameters must respect the following inequation

$$|\omega_0| > \frac{\Delta\omega}{2}. \tag{4}$$

Moreover, ω_0 must be large enough to avoid erroneous positive contrast due to the field inhomogeneities and the broadening of water protons spectrum, in order not to lose the SPM positive contrast specificity.

2.2. Fraction of saturated protons

Intuitively, the ORS contrast must be proportional to the fraction ϕ of water protons saturated by the saturation pulse. This

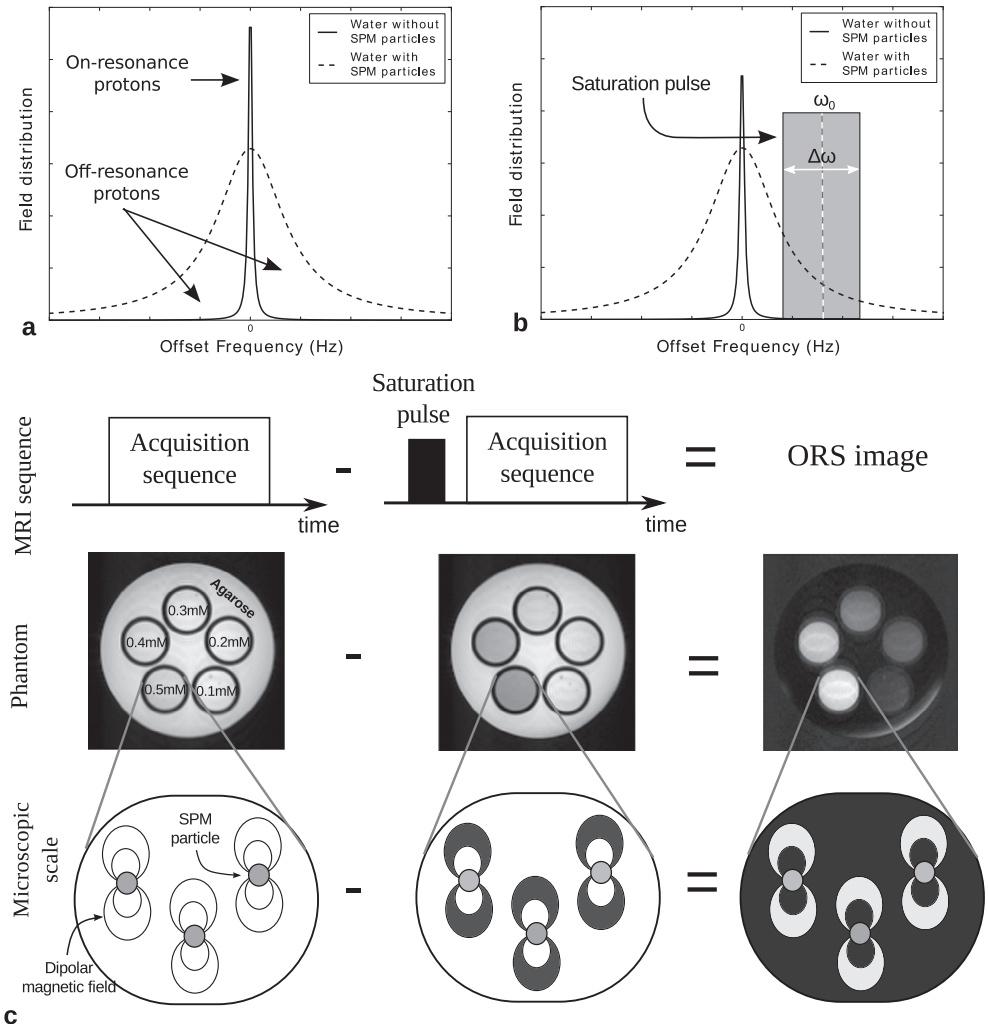

Fig. 2. Principle of the ORS sequence. (a) Larmor frequency distribution of a solution with and without SPM particles. The dipolar magnetic field created by the SPM particles broadens the frequency distribution. (b) The saturation pulse saturates protons near SPM particles. (c) Subtraction of the two MR images obtained on a phantom constituted of SPM particles (VSOP-20 nm) with different concentrations embedded in an agarose gel matrix.

fraction is computed by integrating the magnetic field distribution of a SPM particles solution, given in [56], in the range of the saturation pulse bandwidth. The latter is given by the frequency interval $[\omega_0 + \Delta\omega/2, \omega_0 - \Delta\omega/2]$ (Fig. 2b). After integration, ϕ is given by (see Section 1 of the Supplementary material)

$$\phi(Cc, B_{eq}, \omega_0, \Delta\omega) = \frac{1}{\pi}\left|\arctan\left(a(\omega_0 + \Delta\omega/2)\right) - \arctan\left(a(\omega_0 - \Delta\omega/2)\right)\right| \quad (5)$$

where $a = 1.32\ 10^{-3}/B_{eq}Cc$, Cc is the iron concentration and B_{eq} is the equatorial field of the SPM particles.

The fraction ϕ, plotted in Fig. 3a, is linearly dependent on the iron concentration for low concentrations. At this stage, the regions of saturated protons, situated around the SPM particles, are not superimposed on each other (Fig. 3b). This proportionality is lost when the regions of saturated protons are superimposed, i.e. for high concentrations (Fig. 3c). Fig. 3a also shows that, for a fixed value of ω_0 and according to inequation (4), ϕ is higher when $\Delta\omega$ is close to $2|\omega_0|$. In the same way, for a fixed value of $\Delta\omega$, ϕ increases when the ω_0 value approaches $\Delta\omega/2$. These two last dependences can be understood by analyzing Fig. 2b.

2.3. Analytical expression of the contrast

The image acquisition sequence used in this work is a Fast Imaging with Steady-State Precession (FISP, Fig. S2) [54,57–60]. Our ORS sequence is thus called Off-Resonance Saturation–FISP, or ORS–FISP. The Off-Resonance saturation pulse was composed of a 90° pulse followed by a spoiler gradient. The longitudinal relaxation between the saturation pulse and the imaging sequence was neglected. This is justified by the large T_1 of our samples ($T_1 \approx 3$ s).

The contrast of the ORS–FISP sequence is computed after the first excitation pulse of the FISP sequence because contrast is confined in the middle of the k-space ($k_x = k_y \approx 0$), while the larger value of k_x and k_y are devoted to the spatial resolution [61]. In this work, the k-space is acquired starting at $k_y = 0$ and then for k_y increasing toward higher values. A general expression of the contrast obtained after any of the excitation pulses is given in the Supplementary material. This expression can be used when dummy scans are necessary to reach the signal steady state. It is the case for example if $\alpha > 20°$ (it was verified by our simulations and by experiments).

The contrast on an ORS image is defined by the subtraction of the ORS signal intensity of a region without SPM particles

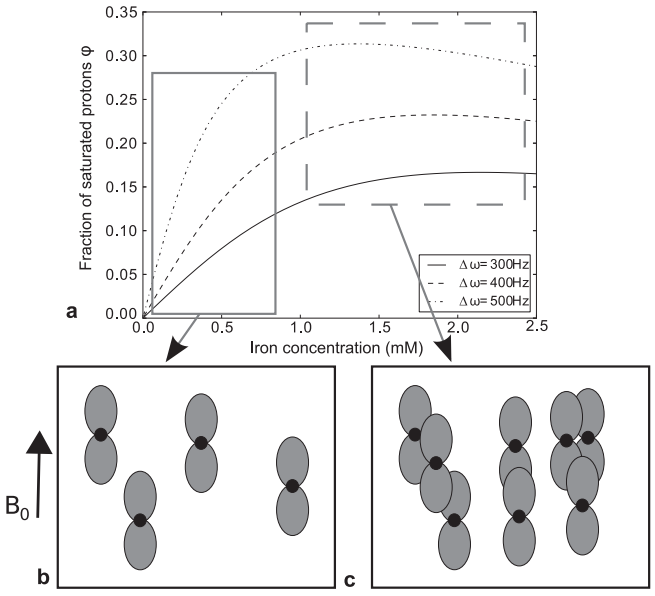

Fig. 3. Influence of the iron concentration (SPM particles) on the fraction ϕ of water protons saturated by the frequency selective saturation pulse for different values of $\Delta\omega$, for $\omega_0 = 300$ Hz. (a) ϕ increases linearly with the particle concentration when the areas of saturated protons are not superimposed (b). This linear behavior is lost when these areas are superimposed (c).

($S_{ORS,no-SPM}$) from the signal of another region containing SPM particles ($S_{ORS,SPM}$):

$$C = S_{ORS,SPM} - S_{ORS,no-SPM} \tag{6}$$

In accordance with the ORS image definition (Fig. 2c), the ORS signal intensities are obtained by subtracting the MRI signal of the image acquired with the saturation pulse ($S_{with\text{-}Sat}$) from the MRI signal of the image acquired without saturation pulse ($S_{without\text{-}Sat}$):

$$S_{ORS} = S_{without\text{-}Sat} - S_{with\text{-}Sat} \tag{7}$$

These MRI signals are given by the transverse component of the magnetization after the first excitation pulse multiplied by the transverse relaxation decay. They are thus calculated as

$$S = M_z^0 \sin\alpha\, e^{-R_2^* TE} \tag{8}$$

where M_z^0 is the longitudinal component of the equilibrium magnetization $M^0 = (0, 0, M_z^0)$, α is the flip angle of the excitation pulse, TE is the echo time and R_2^* is the transverse relaxation rate of the solution.

The signal intensity of the regions without SPM particles is supposed to be unaffected by the saturation pulse (Fig. 2). It is the case if the saturation pulse parameters, ω_0 and $\Delta\omega$, are well chosen and if a highly frequency selective saturation pulse is used (see Section 5). Therefore, the signal intensities on images acquired with and without saturation pulse are equal in these regions, leading to $S_{ORS,no-SPM} = 0$.

To compute the ORS signal of the region containing SPM particles, suppose that the SPM particles are characterized by their relaxivities r_1 and r_2^* (defined as the increase of the relaxation rates R_1' and $R_2^{*\prime}$ respectively when the iron concentration increases of 1 mM). If the diamagnetic relaxation rates of the region without SPM particles are R_1 and R_2^*, the total relaxation rates of the particles suspension are given by

$$\begin{aligned} R_1' &= r_1 Cc + R_1 \\ R_2^{*\prime} &= r_2^* Cc + R_2^* \end{aligned} \tag{9}$$

where Cc is the iron concentration of the particles suspension.

In a region containing SPM particles, the signal on the image acquired without saturation pulse is obtained thanks to Eq. (8) and using the total relaxation rate (9), which gives

$$S_{without\text{-}Sat} = M_z^0 \sin\alpha\, e^{-TE\left(R_2^* + r_2^* Cc\right)}. \tag{10}$$

The signal expression on the image acquired with the saturation pulse is more complex. The saturation pulse destroys the signal coming from a fraction ϕ of protons. Therefore, the signal is only created by the fraction $1 - \phi$ of unsaturated protons. We suppose that the signal decay is the same with and without the saturation pulse application and that the longitudinal relaxation rate is negligible between the saturation pulse and the beginning of the imaging sequence. The signal is thus given by

$$S_{with\text{-}Sat} = (1 - \phi) \sin\alpha\, e^{-TE\left(R_2^* + r_2^* Cc\right)} M_z^0. \tag{11}$$

The ORS–FISP contrast is calculated with Eqs. (6) and (7). As $S_{ORS,no-SPM} = 0$, the contrast is obtained by subtracting (10) from (11), which gives

$$C = \phi \sin\alpha\, e^{-TE\left(R_2^* + r_2^* Cc\right)} M_z^0 \tag{12}$$

This expression shows that the ORS–FISP contrast between area with and without SPM particles is proportional to the fraction of protons saturated by the saturation pulse ϕ. It exponentially decreases with the echo time TE and the SPM particles transverse relaxivity r_2^*. The dependence of the contrast on ω_0 and $\Delta\omega$ is only included in ϕ. The contrast dependence on the particle concentration is more complex.

Note that, as in most MRI sequence theories, noise has not been introduced in our model. However it must be taken into account when theory is compared to experimental results. This can be done by considering a constant noise on the MR images. This assumption is justified because a volume coil is used in this work for the signal acquisition [60]. In this case, Eq. (12) can be multiplied by a constant corrective factor (determined by a fitting of the experimental results) to take the noise, or the standard deviation of the void σ_0, into account. This factor also includes the voxel protons density, present in Eq. (12) through the M_z^0 term. The resulting expression can then be compared to the experimental Contrast to Noise Ratio (CNR).

3. Materials and methods

3.1. Phantoms

Several phantoms were prepared in order to study the ORS–FISP contrast. These phantoms were constituted of a 27 mm-diameter tube filled with 1.5% agarose gel in which five tubes of 6 mm-diameter containing SPM particles dispersed in 1.5% agarose gel were immersed.

All the SPM particles used in this work are composed of magnetite (Fe_3O_4). Five types of samples, divided into two categories, were used. The first category is constituted of VSOP particles purchased from Ferropharm (Teltow, Germany). These are Small Superparamagnetic Particles of Iron Oxide (SPIO) of 3, 10 and 20 nm diameters. The second kind of particles are Micrometer-sized Particles of Iron Oxide (MPIO). They are composed of magnetite crystals embedded in a polymer matrix for a total diameter of 1 μm (for the 1 μm-MPIO) and 3 μm (for the 3 μm-MPIO). They were purchased from ProMag magnetic Microspheres, bangs laboratories, Inc (Indiana, USA).

The iron concentration of the suspensions was determined by ICP-AES (Inductively Coupled Plasma-Atomic Emission

Table 1
SPM particle parameters obtained by relaxometry at 11.7 T and magnetometry (see Supplementary material for more details).

Particles	r_1 ($mM^{-1}\,s^{-1}$)	r_2 ($mM^{-1}\,s^{-1}$)	Mono-crystal radius (nm)	B_{eq} (T)
3 nm-VSOP	2.1	90	3.74	0.13
10 nm-VSOP	2.2	170	5.7	0.12
20 nm-VSOP	2.1	200	4.21	0.13
1 μm-MPIO	~0	600	5.13	0.17
3 μm-MPIO	~0	/	5.14	0.16

Spectroscopy) after microwave digestion of the samples. All the particles were characterized by magnetometry (to obtain the mono-crystal radius and magnetization) and relaxometry on the MRI scanner. The relaxation times of the 1.5% agarose gel (without particles) were respectively $T_1 = 3$ s and $T_2 = 80$ ms.

Results presented in Table 1 show that all the SPM particles are composed of clustered magnetite mono-crystals possessing a radius of 5 nm, except for the 3 nm-VSOP which are constituted of a single magnetite mono-crystal.

3.2. MRI experiments

MR images were acquired on a 11.7 T scanner (Bruker, Biospec, Etlingen, Germany) with a quadrature volume coil (inner diameter of 40 mm). The acquisition sequence used in this work was a Fast Imaging with Steady State precession (FISP, Fig. S2). Two images were acquired for each set of the sequence parameters: an image without and one with the application of an Off-Resonance Saturation (ORS) pulse. These two images were then subtracted pixel by pixel to obtain the ORS–FISP image.

The ORS–FISP sequence parameters were, when not mentioned in the text or in the figure legends, given by TR = 4 ms, TE = 1.5 ms, a flip angle = 10°, matrix size = 128 × 128, FOV = 40 mm, slice thickness = 2 mm, four segments (2 s between each segment) and a number of averages 20. The saturation pulse was a sinc pulse with 3 lobes and a flip angle of 90°. If they are not specified elsewhere, the frequency ω_0 and the bandwidth $\Delta\omega$ of this pulse were $\omega_0 = 300$ Hz and $\Delta\omega = 500$ Hz respectively.

Conventional T_2-weighted images were acquired using a RARE (Rapid Acquisition with Relaxation Enhancement) sequence with TR/TE = 1500/15 ms and a RARE factor of 4.

The results extracted from the ORS–FISP images corresponded to the Contrast to Noise Ratio (CNR) between a region of the phantom containing SPM particles and a region of the same phantom without SPM particles (with only agarose gel). The CNR was defined as

$$\mathrm{CNR} = \frac{S_{\mathrm{ORS,SPM}} - S_{\mathrm{ORS,no-SPM}}}{\sigma_0} \tag{13}$$

where σ_0 is the measured standard deviation of a region outside the phantom. The Regions Of Interest (ROI) were placed manually in a homogeneous area. All the results were expressed as the CNR ± the standard deviation. The image processing was performed with ImageJ (National Institutes of Health, Bethesda, USA).

3.3. Simulations

The simulations developed in this work are based on a microscopic approach, similarly to the T_2 simulations previously described in the literature [62–64]. Their aim is to compute the ORS–FISP contrast between regions with and without SPM particles. For this purpose, simulations need to simulate the MRI signal created by a sample with and without SPM particles, both with and without the application of a saturation pulse. However, the theoretical section predicts that ORS signal is null for the sample without SPM particles. Therefore, the simulation will only compute the ORS signal created by a solution containing SPM particles.

The first simulation step is to create a cubic simulation space composed of randomly distributed spherical and impenetrable SPM particles. A static magnetic field $\vec{B}_0$, aligned with the z axis, was imposed on this space. SPM particles were defined by their radius R_p and their equatorial field B_{eq}. These particles possess a magnetic moment aligned with $\vec{B}_0$ and create a dipolar field given by Eq. (1).

At the beginning of the simulation, several protons, each possessing a protonic magnetic moment $\vec{\mu}$ initially aligned with $\vec{B}_0$, were randomly distributed in the simulation space. The proton diffusion is simulated by a random walk process. At each time step Δt, the proton position $\vec{r}(t)$ was incremented by a vector $\vec{\delta}_m$ randomly oriented:

$$\vec{r}(t_{m+1}) = \vec{r}(t_m) + \vec{\delta}_m, |\vec{\delta}_m| = \sqrt{6D\Delta t}, \tag{14}$$

where D is the protons diffusion coefficient. The time step was equal to $\Delta t = R_p^2/6D$ in order to get a space jump equal to a SPM particle radius. This time step is divided by 8 when the protons were at a distance smaller than $8R_p$ from the center of a SPM particle in order to take into account the strong magnetic inhomogeneities in the SPM particle vicinity.

The time evolution of the proton magnetic moments was computed after each time step using both the Bloch equations and the classical NMR formalism:

$$\begin{cases} \mu_x(t+\Delta t) = [\mu_x(t)\cos\theta + \mu_y(t)\sin\theta]e^{-R_2\Delta t} \\ \mu_y(t+\Delta t) = [\mu_x(t)\sin\theta - \mu_y(t)\cos\theta]e^{-R_2\Delta t} \\ \mu_z(t+\Delta t) = \left(1 - e^{-\Delta t/T_1}\right)M_z^0 + \mu_z(t)e^{-R_1\Delta t} \end{cases} \tag{15}$$

In this last expression, $\theta = \gamma B_{\mathrm{tot}}(t+\Delta t)\Delta t$ and $R_{1,2}$ are respectively the longitudinal and transverse relaxation rates of the solvent containing the SPM particles. $\vec{B}_{\mathrm{tot}}$, which is aligned with the z axis, is the total magnetic field felt by the protons at position $\vec{r}(t)$. It was computed by adding the magnetic field created at position $\vec{r}(t)$ by all the SPM particles to B_0:

$$B_{tot}(\vec{r}(t)) = B_0 + \sum_j B_{dip}\left(\vec{r}(t) - \vec{r}_{SPM,j}\right), \tag{16}$$

where $\vec{r}_{\mathrm{SPM},j}$ is the position of the SPM particle j. The protonic relaxation induced by the SPM particles was not introduced in Eq. (15) because the simulations were built in order to simulate the relaxation [62].

The ORS-FISP sequence was applied to water protons by modeling each pulse by a rotation matrix. The excitation pulse corresponded to a rotation matrix of an angle α around the x-axis. The saturation pulse, applied before the imaging sequence (FISP), was modeled by applying a rotation of 90° on the protons undergoing a frequency shift in the range of the saturation pulse bandwidth. The affected protons were then dephased to spoil their MRI signal.

The global magnetization at a specific time is equal to the average of the N proton magnetic moments at this specific time:

$$\vec{M}(t) = \frac{1}{N}\sum_{i=1}^{N}\vec{\mu}^i(t) \tag{17}$$

The MRI signal at the echo time TE after the first excitation pulse is then given by

$$S(TE) = \sqrt{M_x^2(TE) + M_y^2(TE)} \tag{18}$$

A simulation was performed with the application of a saturation pulse and another one without saturation pulse in order to obtain the ORS contrast. The MRI signals of these two 'images' were then computed using Eqs. (17) and (18). The difference of these signals provided the ORS contrast using Eqs. (6) and (7). As in our analytical theory, noise is not included in the simulations and the contrast value is normalized by the proton density, the contrast is comprised between 0 and 1.

The general simulation parameters used in this work were the same as those of the experiments in order to ease the comparison. When not mentioned elsewhere, the parameters were:

- Temperature: 310 K (human body temperature).
- Diffusion coefficient of water protons : $D = 3 \cdot 10^{-9}\ m^2\ s^{-1}$.
- Magnetization of SPM particles (magnetite): 100 Am^2/kg [Fe], corresponding to $B_{eq} = 0.16$ T.
- Particle radius: 20 nm.
- Relaxation time of the solution containing the SPM particles (agarose gel): $T_1 = 3$ s and $T_2 = 80$ ms.

These parameters led to a simulated transverse SPM particles relaxivity $r_2^* = 600\,mM^{-1}\ s^{-1}$.

All the simulation results presented in this work were obtained by averaging three simulations. The contrast shown in graphs corresponds to the contrast mean and the error bars corresponds to the standard deviation of the three measurements.

The routines were written in C++, parallelized with OPENMP and used the GNU Scientific Library (GSL). The simulations were performed on the resources of the *Consortium des Equipements de Calcul Intensif* (CECI, Université Catholique de Louvain, Université Libre de Bruxelles, Université de Liège, Université de Namur and Université de Mons). Data analysis and graphs were carried out with Python, using the Numpy, Scipy and Matplotlib libraries.

3.4. Quantification of the agreement between simulations, experiment and theory

The agreement between the simulation (or the experimental) results and the theoretical predictions was quantified by the calculation of the coefficient of determination R^2. To compute R^2, graphs representing the simulation (or the experimental) results as a function of the theoretical predictions were first plotted. These graphs should show a linear relationship with a slope equal to 1. The coefficient of determination was then calculated as [65]

$$R^2 = 1 - \frac{\sum_{i=1}^{n}(y_i - \hat{y}_i)^2}{\sum_{i=1}^{n}(y_i - \bar{y})^2} \tag{19}$$

where y_i are the experimental (or the simulation) values of the contrast, $\underset{i}{\widehat{y}}$ are the theoretical values of the contrast and $\bar{y} = \frac{1}{n}\sum_{i=1}^{n} y_i$ is the mean of the experimental (or the simulation) values. A coefficient equal to 1 indicates a perfect regression.

4. Results

4.1. Influence of the iron concentration on the ORS contrast

Numerical simulations and MR images of phantoms containing 1 μm-MPIO in different concentrations were employed to investigate the influence of the iron concentration on the contrast (Fig. 4). MR images and numerical simulations were performed for different values of ω_0 with $\Delta\omega = 500$ Hz, fulfilling condition (4).

The numerical simulation results and the theoretical predictions are shown on Fig. 4a. A good agreement was observed between theory and simulations for all values of ω_0. Indeed, the coefficient of determination R^2, calculated with Eq. (19), was between 0.95 and 0.99 for all ω_0 values. Theory and simulations showed a contrast increase with iron concentration until a maximum value was reached. The contrast then decreased for increasing iron concentration. This result shows the existence of an optimal iron concentration maximizing contrast.

MR images acquired with the ORS–FISP sequence (Fig. 4b) clearly showed positive contrast where SPM particles were located. The ORS–FISP contrast increased with iron concentration for all values of ω_0. On the contrary, the T_2-weighted image (RARE) showed black spots for SPM particles with a decrease of signal intensity for increasing iron concentration.

The CNR calculated from phantoms containing 1 μm-MPIO (Fig. 4c) was consistent with the numerical simulations results and theoretical predictions. CNR increased until a maximum was reached, after which it decreased. This behavior was observed for all values of ω_0.

Theoretical predictions are plotted on Fig. 4c. The curves were obtained with Eq. (12) using the experimental parameters of the 1 μm-MPIO (Table 1) and the MRI sequence parameters. As these SPM particles were composed of aggregated iron oxide mono-crystals, their parameters should be adapted to compare the experimental results to the theoretical predictions. However, the Section 2.4 of the Supplemental materials shows that the mono-crystal parameters (presented on Table 1) can be directly introduced in Eq. (12). All the curves were multiplied by the same corrective factor to take into account the noise and the spin density. A good agreement between theory and experiments was observed for all ω_0 values ($R^2 \sim 0.81$–0.85) – even if the experimental results seemed to be systematically smaller than the theoretical predictions for iron concentration below 0.4 mM with $\omega_0 = 300Hz$. Similar results were obtained with the 3 nm-VSOP (see Fig. S4 of the Supplementary material).

The contrast behavior can be explained thanks to Eq. (12). For small iron concentration Cc, the exponential term of Eq. (12) can be approximated by $e^{-TE(r_2^* Cc + R_2)} \approx e^{-R_2 TE}$. The only contrast dependence on the iron concentrations is thus included in ϕ at this stage. As ϕ is linear with Cc for small concentrations (Fig. 3a and b), the contrast is thus linear with Cc for small Cc. In opposite, at high iron concentrations, the exponential term of Eq. (12) is dominant, implying a contrast decrease for increasing Cc above a limit concentration value. This latter corresponds to an optimum concentration for which the contrast is maximum.

4.2. Influence of the saturation pulse offset ω_0 on the contrast

The numerical simulations and MR images of phantoms containing 1 μm-MPIO results presented on (Fig. 4) were also used to investigate the influence of ω_0 on the contrast. Numerical simulations, in agreement with the theoretical predictions, revealed that a higher contrast was obtained when ω_0 was close to $\Delta\omega/2$ (that is equal to 250 Hz) for all iron concentrations (Fig. 4a). This prediction was congruent with the ORS–FISP images (Fig. 4b). Indeed, a better contrast was observed for $\omega_0 = 300$ Hz than for $\omega_0 = 450$ Hz. The computed CNR confirmed this observation (Fig. 4c): for all iron concentrations, CNR increased when ω_0 was close to $\Delta\omega/2$. The theoretical predictions interpolated well the experimental data. Similar results were obtained for 3 nm-VSOP particles (see Fig. S4 of the Supplementary material).

Theoretically, the contrast increase observed when ω_0 was close to $\Delta\omega/2$ is caused by the increase of ϕ when $\omega_0 \to \Delta\omega/2$ (Fig. 2 and Eq. (5)). Indeed, contrast is proportional to ϕ and the ORS contrast only depends on ω_0 through ϕ (Eq. (12)).

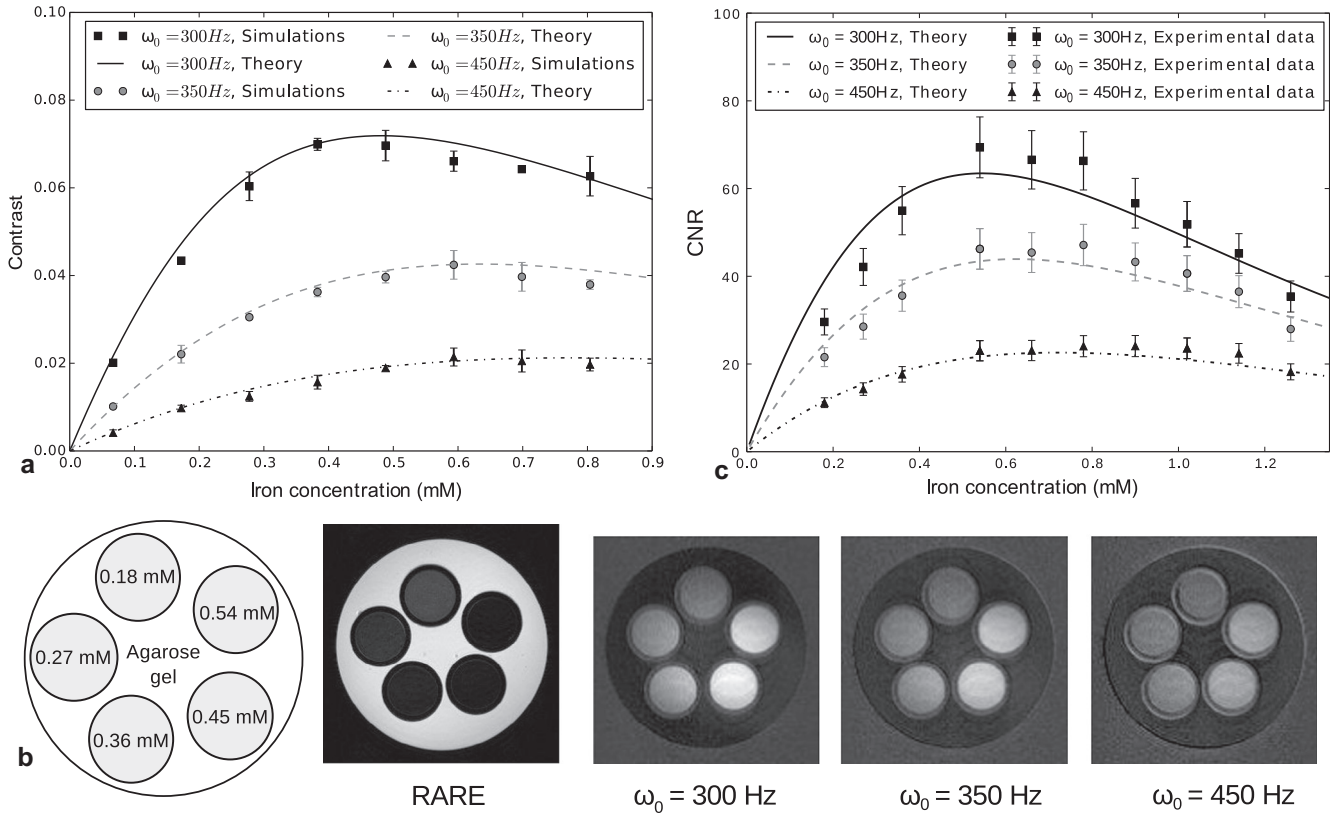

Fig. 4. Influence of the iron concentration on the contrast for different values of saturation pulse offset ω_0. (a) Numerical simulations results and theoretical predictions. (b) MR images of a phantom containing different concentrations of 1 μm-MPIO acquired with a RARE and the ORS-FISP sequence. (c) CNR estimated from MR images of phantoms containing 1 μm-MPIO and theoretical predictions.

4.3. Influence of the saturation pulse bandwidth $\Delta\omega$ on the contrast

ORS–FISP contrast was studied by numerical simulations and MRI experiments for different values of $\Delta\omega$ respecting condition (4) (Fig. 5). The phantoms were again constituted of 1 μm-MPIO with different iron concentrations.

The numerical simulation results and the theoretical predictions, which were in good agreement ($R^2 \sim 0.95$–0.99), are shown in Fig. 5a. A higher contrast was observed when $\Delta\omega$ was close to $2\omega_0$ (600 Hz) for all iron concentrations. For all values of $\Delta\omega$, the contrast dependence on the iron concentration was in agreement with the behavior reported in previous section.

ORS–FISP images (Fig. 5b), which showed positive contrast where the SPM particles were situated, also showed that the contrast increased when $\Delta\omega$ approached $2\omega_0$. Indeed, the contrast obtained for $\Delta\omega = 500$ Hz was higher than for $\Delta\omega = 300$ Hz. The corresponding RARE image showed black spots where the SPM particles were situated (Fig. 5b).

The CNR extracted from ORS–FISP images (Fig. 5c) confirmed the simulation results. Indeed, the CNR increased when $\Delta\omega$ was close to $2\omega_0$ for all values of iron concentration. The theoretical predictions, estimated with Eq. (12) using the experimental parameters (Table 1), were in good agreement with the experimental results (except for one point at 0.36 mM for $\Delta\omega = 500$ Hz). Indeed, the coefficient of determination was between 0.81 and 0.86 for all the $\Delta\omega$ values. As before, all the curves were scaled by the same corrective factor to take the noise into account. Similar results were obtained for 3 nm-VSOP (see Fig. S5 of the Supplementary material).

The contrast increase when $\Delta\omega$ was close to $2\omega_0$ can be explained thanks to Fig. 2. The fraction ϕ of saturated protons increases when the $\Delta\omega$ value approaches $2\omega_0$. As the contrast is proportional to ϕ, and as $\Delta\omega$ affects the contrast only through ϕ (see Eq. (12)), this effect logically induces a contrast increase when $\Delta\omega$ gets large.

4.4. Influence of the echo time TE

MR images of a phantom containing different concentrations of 1 μm-MPIO and numerical simulations were performed using different echo times *TE* to analyze its effect on the contrast (Fig. 6). All these results were obtained with a repetition time of 15 ms.

The contrast calculated from the numerical simulations (Fig. 6a) decreased with the increase of *TE*. This decrease was observed for all iron concentrations, especially for high concentrations. The contrast dependence on iron concentration was similar as in the previous sections. Fig. 6a also shows that the optimal iron concentration (corresponding to the maximum contrast) decreased when *TE* increased. As before, the theoretical predictions were in good agreement with the simulations results ($R^2 \sim 0.95$–0.99 for all the *TE* values).

The ORS–FISP images acquired with different values of *TE* are presented on Fig. 6b. The contrast clearly decreased for increasing *TE*, especially for high iron concentration. A larger amount of noise was observed on the MR image acquired with *TE* = 4.5 ms due to the decrease of the signal intensity with the echo time.

Fig. 6c presents the CNR extracted from the ORS–FISP images of phantoms containing 1 μm-MPIO particles. The theoretical predictions, calculated with Eq. (12) using the 1 μm-MPIO characteristics (Table 1) and the ORS–FISP sequence parameters, are also plotted on Fig. 6c. All the curves were scaled by the same correcting factor. A good agreement between theory and experiments was observed

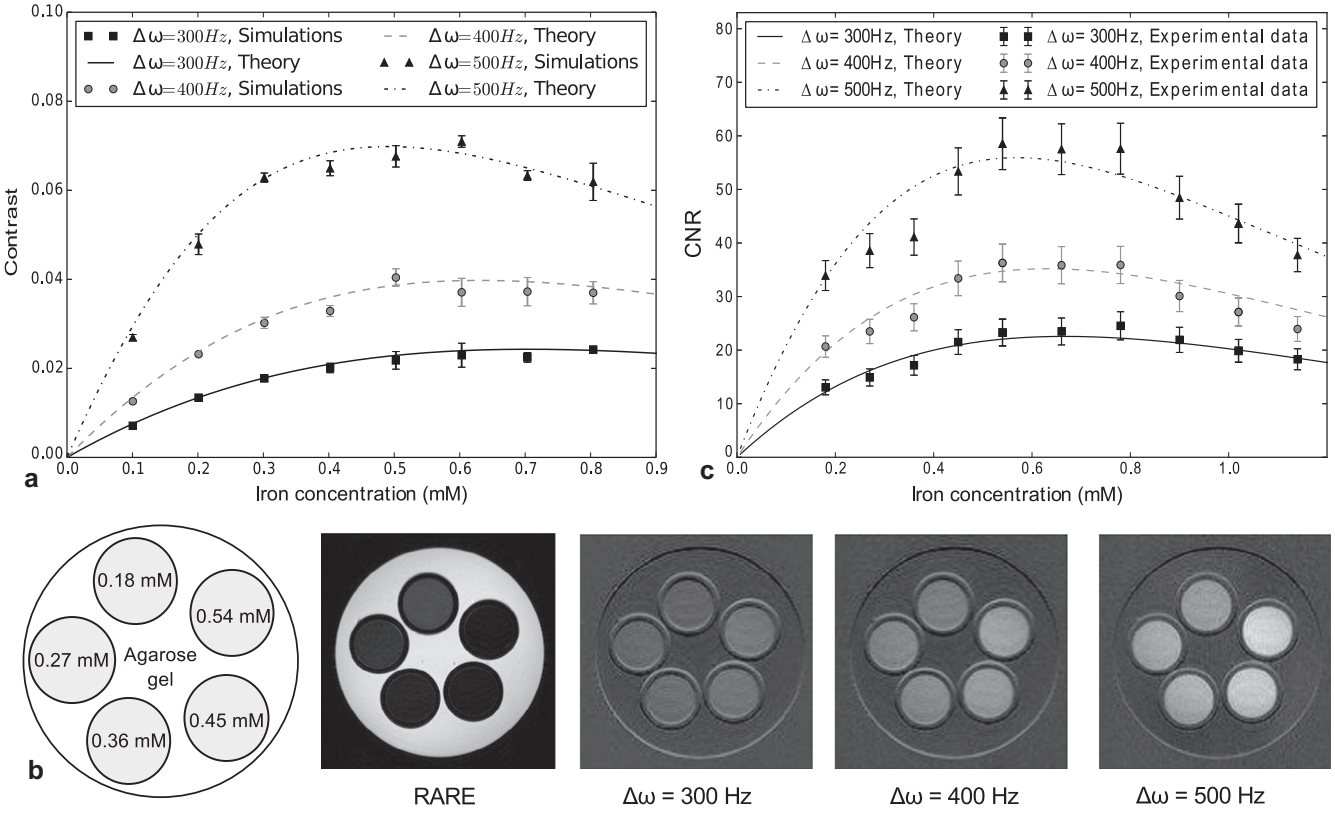

Fig. 5. Influence of the iron concentration on the contrast for different values of saturation pulse bandwidth $\Delta\omega$, with $\omega_0 = 300$ Hz. (a) Numerical simulations results and theoretical predictions. (b) RARE and ORS-FISP images acquired with different $\Delta\omega$ values for a phantom containing different concentrations of 1 μm-MPIO. (c) CNR extracted from ORS-FISP images of phantoms constituted of 1 μm-MPIO in different concentrations and theoretical predictions.

($R^2 \sim 0.81$–0.86). The results were similar to those obtained with numerical simulations. CNR was higher for low values of *TE*. Moreover, as predicted by simulations and theory, the optimum iron concentration depended on *TE*. Similar results were observed for the 3 nm-VSOP (see Fig. S6 of the Supplementary material).

The contrast dependence on *TE* can be explained by the theoretical model. Eq. (12) reveals that the contrast is exponentially dependent on the echo time. This dependence is due to the exponential decay of the transverse MRI signal after the excitation pulse, remembering that the signal is acquired after a time *TE*.

4.5. Optimal SPM particles for ORS–FISP

A phantom composed of five types of SPM particles (3 nm-VSOP, 10 nm-VSOP, 20 nm-VSOP, 1 μm-MPIO and 3 μm-MPIO), with the same iron concentration of 0.75 mM, was prepared in order to evaluate the influence of the particle characteristics on the contrast obtained with the ORS–FISP sequence. The theoretical model predicts that only the equatorial field B_{eq} and the SPM particles relaxivities r_1 and r_2^* influence the ORS–FISP contrast.

All the SPM particles were constituted of magnetite crystals with approximately the same equatorial field and had a practically null longitudinal relaxivity at 11.7 T. However, they presented different transverse relaxivities r_2 at 11.7 T (Table 1). Therefore, r_2^* is the only property of the particles that influences contrast for our samples.

Numerical simulations were performed with SPM particles presenting different r_2^* (Fig. 7a). Results were compared to the theoretical predictions. A good agreement was observed between theory and simulations ($R^2 = 0.94$). Both of them predicted an exponential decrease of the contrast for increasing r_2^*.

MR images acquired with a RARE, a simple FISP (without saturation pulse) and the ORS–FISP sequence are presented on Fig. 7b. The RARE image, T_2-weigthed, showed black spots where the SPM particles were situated. The FISP image was T_2-weigthed due to the small *TR* (4 ms) and to the value of $r_1 \approx 0$ for our SPM particles. This image presented black spots for MPIO particles and no contrast for the VSOP. It showed that all VSOP particles had similar r_2^*, smaller than the MPIO particles r_2^*.

The ORS–FISP image clearly showed a higher signal for the VSOP particles than for the MPIO. This observation was confirmed by the CNR extracted from the MR image, plotted on Fig. 7c. This behavior was consistent with the simulation and theoretical results (Fig. 7a). Indeed, MPIO possess a higher r_2^* than the VSOP particles (see Table 1 and the FISP image of the Fig. 7b). It can be noted that similar contrast is observed for the different VSOP samples. This can be due to the relatively small r_2^* value difference for these samples (Table 1).

The ORS–FISP contrast dependence on r_2^* can be theoretically understood. Eq. (12) shows that the contrast is exponentially dependent on r_2^*, as shown in Fig. 7a. The higher the r_2^* is, the faster the signal decreases after the excitation pulse. This implies a low MRI signal for SPM particles possessing a large r_2^*. Therefore, SPM particles possessing low r_2^* must be preferred to optimize the contrast obtained with the ORS–FISP sequence.

5. Discussion

The ORS sequence combined with a FISP imaging sequence was studied with numerical simulations and experiments on agarose gel phantoms with a 11.7T MRI scanner. A theoretical model able to predict the ORS–FISP contrast in function of the sequence

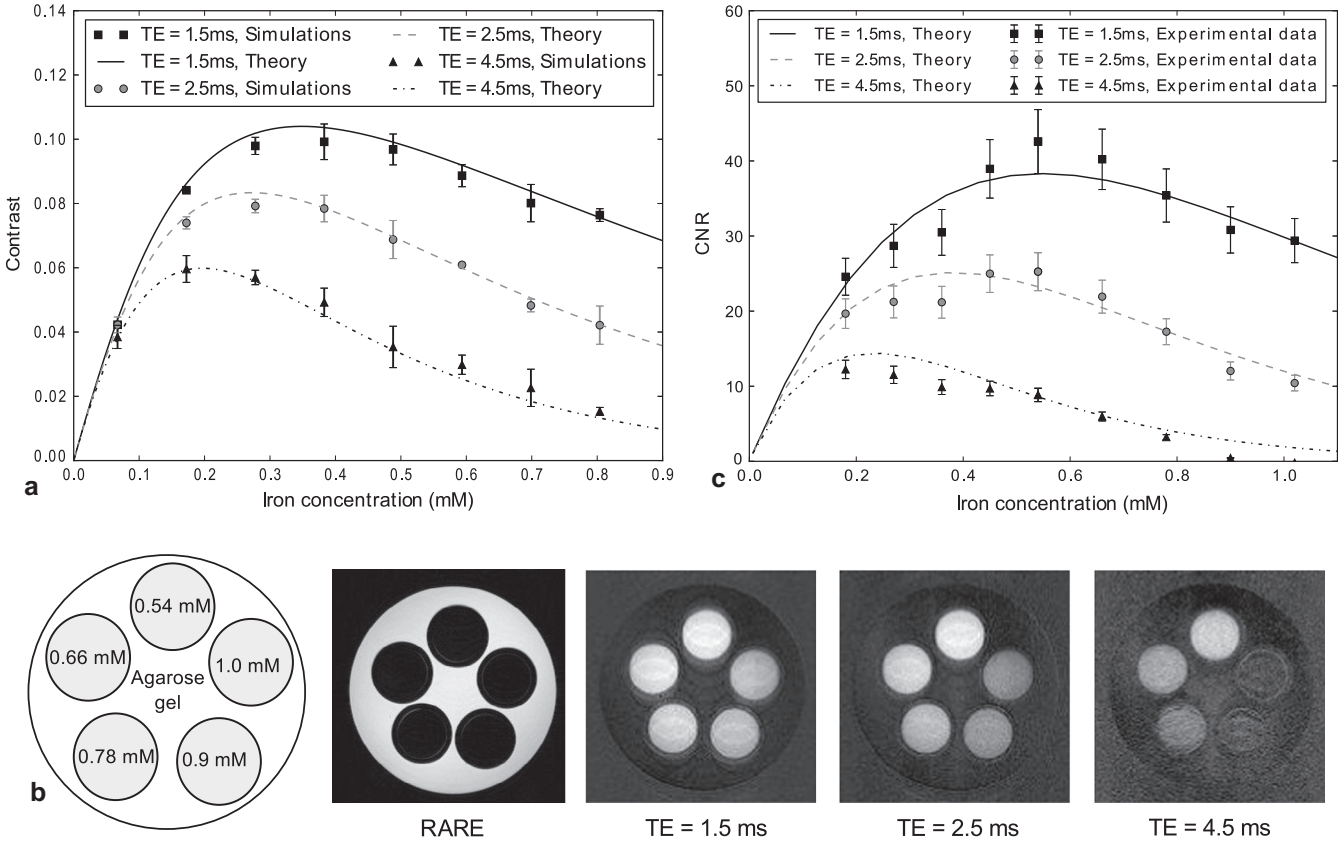

Fig. 6. Influence of the iron concentration on the ORS-FISP contrast for different values of echo time *TE*. (a) Numerical simulations results compared to the theoretical predictions. (b) MR images acquired with a RARE and the ORS-FISP sequence using different *TE* for a phantom containing different concentrations of 1 μm-MPIO. (c) CNR extracted from ORS-FISP images of phantoms constituted of 1 μm-MPIO in different concentrations and theoretical predictions.

parameters and the SPM particles properties was developed. The model supposes that the magnetic field is high enough – i.e. the SPM particles magnetization is saturated (see Fig. S3) and the longitudinal relaxivity of the SPM particles can be neglected [19]. These conditions are fulfilled for any field higher than 1 T. The theoretical predictions and simulations results were in good agreement with the experimental results, which shows that the theory and the simulations can be used to optimize the sequence parameters. The theory can also be used to predict the contrast obtained with aggregated nanoparticles.

The ORS–FISP created a sufficient contrast with low iron concentration (~0.5 mM), which could be reached in *in vivo* applications. The simulations, experimental results and theory revealed a non-linearity between the iron concentration and the contrast, as already noted in [52]. This behavior leads to an optimal iron concentration which can be predicted by the theory.

The best saturation pulse parameters were a high pulse bandwidth $\Delta\omega$ combined with a saturation pulse frequency offset $|\omega_0|$ approaching $\Delta\omega/2$ (this behavior has already been shown in [51,52]). However, for a fixed value of $\Delta\omega$, $|\omega_0|$ must be large enough to leave the on-resonance protons unsaturated and to avoid the artifact formation. Therefore, the saturation pulse parameters are a compromise between the amount of contrast and the contrast specificity. In this work, a good compromise was $\omega_0 = 300$ Hz and $\Delta\omega = 400$ Hz. Note that, contrarily to the sequence developed by Zurkiya [52], the pulses used in our work can be considered to be short: diffusion will thus have less effect on the ORS–FISP contrast than in [52].

Results also revealed that a low echo time must be preferred to maximize the contrast. In addition, an increase of echo time leads to a noise increase in the final image, as it can be seen on Fig. 6b. Finally, the maximum ORS contrast was obtained with SPM particles presenting a low transverse relaxivity.

The good agreement between the theoretical predictions, the simulation results and the experimental data shows that theory and simulation are two interesting tools to study the ORS sequence. Moreover, theory and simulations can be adapted to predict the contrast obtained with other imaging sequences, as a spin-echo or a RARE sequence.

However, our theory needs to be adapted to *in vivo* conditions – as nanoparticle internalization in cells, additional magnetic field inhomogeneities (produced by the tissues interface for example) or a different r_2^* value. Such a theoretical model would enable the SPM particles quantification *in vivo*, which could be useful for applications in molecular and cellular imaging.

The optimization of the ONRS–FISP sequence parameters provided in this work could be qualitatively applied for *in vivo* situations. For example, the best SPM particles should present low r_2^* and an optimal SPM particles concentration should still exist. The saturation pulse parameters, ω_0 and $\Delta\omega$, should nevertheless be adapted in order to avoid erroneous positive contrast caused by additional field inhomogeneities.

For *in vivo* applications, another problem concerns the MR image noise. In our work, we considered a constant noise on the image, which is justified by the use of a volume coil [60]. However, other coils, as array coils, should induce a variation of the noise on the MR image. This will have to be taken into account when trying to apply the ORS–FISP sequence *in vivo*.

Finally, the ORS method suffers of some disadvantages. First, the acquisition of two consecutive images can be a limitation because

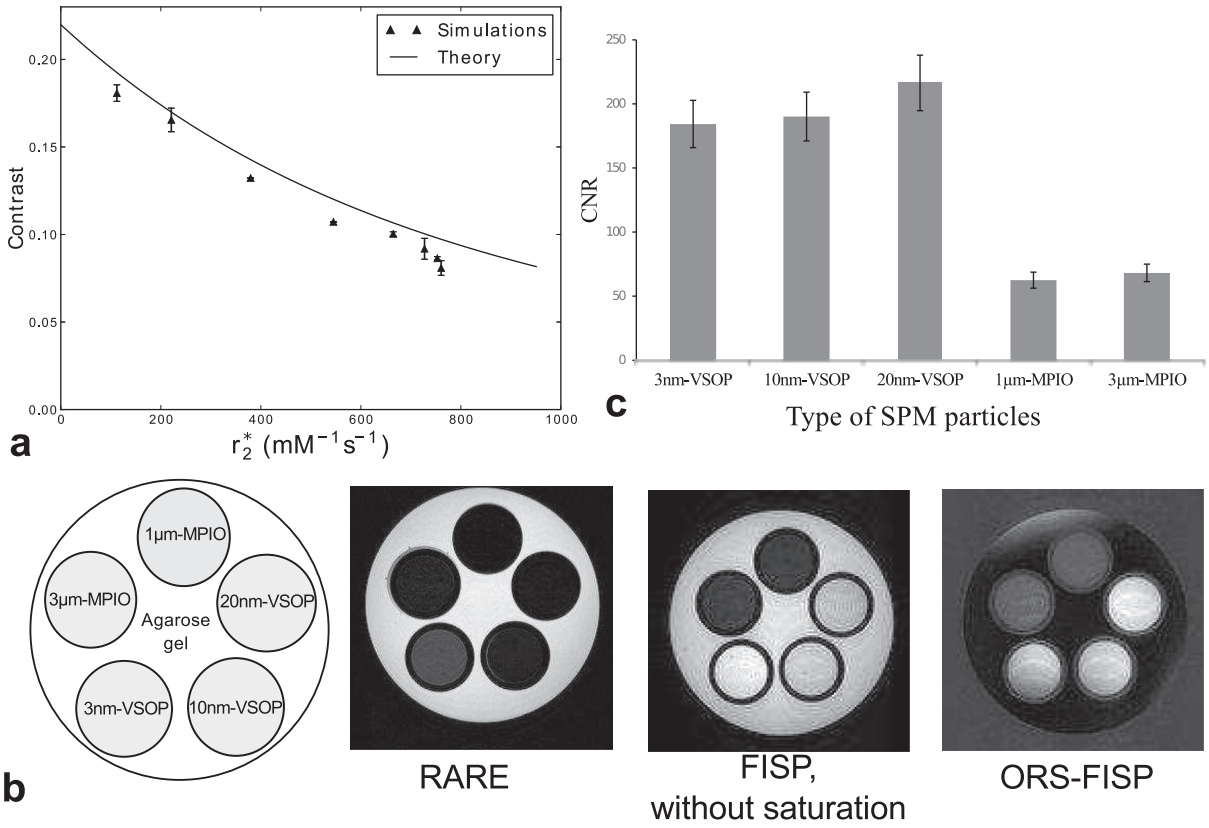

Fig. 7. Influence of SPM particles properties on the ORS-FISP contrast. (a) Numerical simulation results and theoretical predictions of the effect of SPM particles transverse relaxivity on ORS-FISP contrast. (b) MR images (RARE, FISP without saturation pulse and ORS-FISP) of a phantom composed of five different SPM particles at an iron concentration of 0.75 mM. (c) CNR extracted from the MR image presented in b.

of motion artifact. This problem can be minimized because the ORS-FISP sequence is rather fast (about 4 s). Secondly, other sources as tissues interfaces or magnetic field inhomogeneities can produce off-resonance signals, which can lead to erroneous positive contrast and thus, affect the SPM particles detectability. These artifacts can be identified by comparing two MR images obtained with different pulse parameters [40].

6. Conclusion

This work presents a theoretical study of the ORS (Off-Resonance Saturation) sequence coupled with a FISP (Fast Imaging with Steady state Precession) imaging sequence, which provides positive contrast with SPM particles. This sequence was studied with a new numerical simulation protocol and with MRI experiments on agarose gel phantoms containing SPM particles. An analytical expression able to predict the ORS contrast in function of the sequence parameters and particles properties was developed. The theoretical predictions were shown to be in good agreement with the simulation and experimental results. A maximum contrast value was achieved with SPM particles presenting a low transverse relaxivity and for short echo times. The saturation pulses parameters must adapted to saturate as many protons as possible. However, the parameters must be chosen in order not to affect the on-resonance protons, which would create erroneous positive contrast. Finally, an optimal SPM particles concentration, for which the contrast is maximum, was observed and predicted by the theoretical model. Further investigations should be carried out on SPM particles loaded cells and *in vivo* to improve the ORS sequence for practical applications. The theoretical model and the simulations could be adapted for these situations. Such a study could help to develop the quantification of the particles *in vivo*.

Acknowledgments

The authors would like to thank Dr. Alain Roch for helpful discussions and the Biomedical Magnetic Resonance Research Group (UCL) members for their help on the MRI scanner, especially N. Joudiou for his help for the B_1-mapping. S. Delangre (F.R.S.-FNRS Research Fellow) acknowledges the F.R.S.-FNRS for their financial support. This research used resources from the *'Consortium des Équipements de Calcul Intensif'* (CECI); a consortium of high-performance computing centers of UCL, ULB, ULg, UMons (Belgium), and UNamur funded by F.R.S.-FNRS.

Appendix A. Supplementary material

Supplementary data associated with this article can be found, in the online version, at http://dx.doi.org/10.1016/j.jmr.2015.02.014.

References

[1] M.A. Bernstein, Handbook of MRI Pulse Sequences, Academic Press, Amsterdam, Boston, 2004.
[2] Y. Gossuin, A. Hocq, P. Gillis, Q.L. Vuong, Physics of magnetic resonance imaging: from spin to pixel, J. Phys. Appl. Phys. 43 (2010), http://dx.doi.org/10.1088/0022-3727/43/21/213001.
[3] Z. Zhou, Z.-R. Lu, Gadolinium-Based Contrast Agents for MR Cancer Imaging, Wiley Interdiscip. Rev. Nanomed. Nanobiotechnol. 5 (2013) 1–18, http://dx.doi.org/10.1002/wnan.1198.
[4] Y.X. Wang, S.M. Hussain, G.P. Krestin, Superparamagnetic iron oxide contrast agents: physicochemical characteristics and applications in MR imaging, Eur. Radiol. 11 (2001) 2319–2331, http://dx.doi.org/10.1007/s003300100908.

[5] C. Corot, P. Robert, J.-M. Idée, M. Port, Recent advances in iron oxide nanocrystal technology for medical imaging, Adv. Drug Deliv. Rev. 58 (2006) 1471–1504, http://dx.doi.org/10.1016/j.addr.2006.09.013.
[6] S. Laurent, D. Forge, M. Port, A. Roch, C. Robic, L. Vander Elst, R.N. Muller, Magnetic iron oxide nanoparticles: synthesis, stabilization, vectorization, physicochemical characterizations, and biological applications, Chem. Rev. 108 (2008) 2064–2110, http://dx.doi.org/10.1021/cr068445e.
[7] J. Kolosnjaj-Tabi, C. Wilhelm, O. Clément, F. Gazeau, Cell labeling with magnetic nanoparticles: opportunity for magnetic cell imaging and cell manipulation, J. Nanobiotechnol. 11 (2013) S7.
[8] J. Cai, X. Zhang, X. Wang, C. Li, G. Liu, In vivo MR imaging of magnetically labeled mesenchymal stem cells transplanted into rat liver through hepatic arterial injection, Contrast Media Mol. Imaging. 3 (2008) 72–77, http://dx.doi.org/10.1002/cmmi.231.
[9] J.W.M. Bulte, D.L. Kraitchman, Iron oxide MR contrast agents for molecular and cellular imaging, NMR Biomed. 17 (2004) 484–499, http://dx.doi.org/10.1002/nbm.924.
[10] A. Luciani, S. Dechoux, V. Deveaux, M. Poirier-Quinot, N. Luciani, M. Levy, S. Ballet, S. Manin, C. Péchoux, G. Autret, O. Clément, A. Rahmouni, A. Mallat, C. Wilhem, S. Lotersztajn, F. Gazeau, Adipose tissue macrophages: MR tracking to monitor obesity-associated inflammation, Radiology 263 (2012) 786–793.
[11] S.G. Ruehm, C. Corot, P. Vogt, S. Kolb, J.F. Debatin, Magnetic resonance imaging of atherosclerotic plaque with ultrasmall superparamagnetic particles of iron oxide in hyperlipidemic rabbits, Circulation 103 (2001) 415–422.
[12] P. Smirnov, E. Lavergne, F. Gazeau, M. Lewin, A. Boissonnas, B.-T. Doan, B. Gillet, C. Combadière, B. Combadière, O. Clément, In vivo cellular imaging of lymphocyte trafficking by MRI: a tumor model approach to cell-based anticancer therapy, Magn. Reson. Med. 56 (2006) 498–508, http://dx.doi.org/10.1002/mrm.20996.
[13] P. Smirnov, M. Poirier-Quinot, C. Wilhelm, E. Lavergne, J.-C. Ginefri, B. Combadière, O. Clément, L. Darrasse, F. Gazeau, In vivo single cell detection of tumor-infiltrating lymphocytes with a clinical 1.5 Tesla MRI system, Magn. Reson. Med. 60 (2008) 1292–1297, http://dx.doi.org/10.1002/mrm.21812.
[14] D. Forge, S. Laurent, Y. Gossuin, A. Roch, L. Vander Elst, R.N. Muller, An original route to stabilize and functionalize magnetite nanoparticles for the ranosis applications, J. Magn. Magn. Mater. 323 (2011) 410–415, http://dx.doi.org/10.1016/j.jmmm.2010.09.031.
[15] T. Ninjbadgar, D.F. Brougham, Epoxy ring opening phase transfer as a general route to water dispersible superparamagnetic Fe_3O_4 nanoparticles and their application as positive MRI contrast agents, Adv. Funct. Mater. 21 (2011) 4769–4775, http://dx.doi.org/10.1002/adfm.201101371.
[16] Y. Liu, K. Yang, L. Cheng, J. Zhu, X. Ma, H. Xu, Y. Li, L. Guo, H. Gu, Z. Liu, PEGylated FePt@Fe_2O_3 core-shell magnetic nanoparticles: potential theranostic applications and in vivo toxicity studies, Nanomed. Nanotechnol. Biol. Med. 9 (2013) 1077–1088, http://dx.doi.org/10.1016/j.nano.2013.02.010.
[17] C. Boyer, M.R. Whittaker, V. Bulmus, J. Liu, T.P. Davis, The design and utility of polymer-stabilized iron-oxide nanoparticles for nanomedicine applications, NPG Asia Mater. 2 (2010) 23–30, http://dx.doi.org/10.1038/asiamat.2010.6.
[18] Q.L. Vuong, J.-F. Berret, J. Fresnais, Y. Gossuin, O. Sandre, A universal scaling law to predict the efficiency of magnetic nanoparticles as MRI T2-contrast agents, Adv. Health. Mater. 1 (2012) 502–512, http://dx.doi.org/10.1002/adhm.201200078.
[19] Y. Gossuin, P. Gillis, A. Hocq, Q.L. Vuong, A. Roch, Magnetic resonance relaxation properties of superparamagnetic particles, Wiley Interdiscip. Rev. Nanomed. Nanobiotechnol. 1 (2009) 299–310.
[20] A. Roch, R.N. Muller, P. Gillis, Theory of proton relaxation induced by superparamagnetic particles, J. Chem. Phys. 110 (1999) 5403, http://dx.doi.org/10.1063/1.478435.
[21] A.A.M. Elsherbini, A. El-Shahawy, Effect of SPIO nanoparticle concentrations on temperature changes for hyperthermia via MRI, J. Nanomater. 2013 (2013), http://dx.doi.org/10.1155/2013/467878.
[22] B. Blasiak, F.C.J.M. van Veggel, B. Tomanek, Applications of nanoparticles for MRI cancer diagnosis and therapy, J. Nanomater. 2013 (2013) 1–12, http://dx.doi.org/10.1155/2013/148578.
[23] X.-H. Peng, X. Qian, H. Mao, A.Y. Wang, Targeted magnetic iron oxide nanoparticles for tumor imaging and therapy, Int. J. Nanomed. 3 (2008) 311.
[24] M.G. Harisinghani, J. Barentsz, P.F. Hahn, W.M. Deserno, S. Tabatabaei, C.H. van de Kaa, J. de la Rosette, R. Weissleder, Noninvasive detection of clinically occult lymph-node metastases in prostate cancer, N. Engl. J. Med. 348 (2003) 2491–2499.
[25] B. Chertok, B.A. Moffat, A.E. David, F. Yu, C. Bergemann, B.D. Ross, V.C. Yang, Iron oxide nanoparticles as a drug delivery vehicle for MRI monitored magnetic targeting of brain tumors, Biomaterials 29 (2008) 487–496, http://dx.doi.org/10.1016/j.biomaterials.2007.08.050.
[26] C. Sun, J.S.H. Lee, M. Zhang, Magnetic nanoparticles in MR imaging and drug delivery, Adv. Drug Deliv. Rev. 60 (2008) 1252–1265, http://dx.doi.org/10.1016/j.addr.2008.03.018.
[27] M. Wolters, M. Oostendorp, B.F. Coolen, M.J. Post, J.M.H. Janssen, G.J. Strijkers, M.E. Kooi, K. Nicolay, W.H. Backes, Efficacy of positive contrast imaging techniques for molecular MRI of tumor angiogenesis: positive contrast molecular MRI, Contrast Media Mol. Imaging 7 (2012) 130–139, http://dx.doi.org/10.1002/cmmi.471.
[28] W. Liu, H. Dahnke, E.K. Jordan, T. Schaeffter, J.A. Frank, In vivo MRI using positive-contrast techniques in detection of cells labeled with superparamagnetic iron oxide nanoparticles, NMR Biomed. 21 (2008) 242–250, http://dx.doi.org/10.1002/nbm.1187.
[29] C. Lin, S. Cai, J. Feng, Positive contrast imaging of SPIO nanoparticles, J. Nanomater. 2012 (2012) 1–9, http://dx.doi.org/10.1155/2012/734842.
[30] E.-J.P.A. Vonken, M. Schär, J. Yu, C.J.G. Bakker, M. Stuber, Direct in vitro comparison of six three-dimensional positive contrast methods for susceptibility marker imaging, J. Magn. Reson. Imaging 38 (2013) 344–357, http://dx.doi.org/10.1002/jmri.23976.
[31] C.H. Cunningham, T. Arai, P.C. Yang, M.V. McConnell, J.M. Pauly, S.M. Conolly, Positive contrast magnetic resonance imaging of cells labeled with magnetic nanoparticles, Magn. Reson. Med. 53 (2005) 999–1005, http://dx.doi.org/10.1002/mrm.20477.
[32] P. Balchandani, M. Yamada, J. Pauly, P. Yang, D. Spielman, Self-refocused spatial–spectral pulse for positive contrast imaging of cells labeled with SPIO nanoparticles, Magn. Reson. Med. 62 (2009) 183–192, http://dx.doi.org/10.1002/mrm.21973.
[33] Y. Suzuki, C.H. Cunningham, K. Noguchi, I.Y. Chen, I.L. Weissman, A.C. Yeung, R.C. Robbins, P.C. Yang, In vivo serial evaluation of superparamagnetic iron-oxide labeled stem cells by off-resonance positive contrast, Magn. Reson. Med. 60 (2008) 1269–1275, http://dx.doi.org/10.1002/mrm.21816.
[34] M. Stuber, W.D. Gilson, M. Schär, D.A. Kedziorek, L.V. Hofmann, S. Shah, E.J. Vonken, J.W. Bulte, D.L. Kraitchman, Positive contrast visualization of iron oxide-labeled stem cells using inversion-recovery with ON-resonant water suppression (IRON), Magn. Reson. Med. 58 (2007) 1072–1077.
[35] G. Korosoglou, L. Tang, D. Kedziorek, K. Cosby, W.D. Gilson, E.-J. Vonken, M. Schär, D. Sosnovik, D.L. Kraitchman, R.G. Weiss, R. Weissleder, M. Stuber, Positive contrast MR-lymphography using inversion recovery with ON-resonant water suppression (IRON), J. Magn. Reson. Imaging 27 (2008) 1175–1180, http://dx.doi.org/10.1002/jmri.21337.
[36] C.T. Farrar, G. Dai, M. Novikov, A. Rosenzweig, R. Weissleder, B.R. Rosen, D.E. Sosnovik, Impact of field strength and iron oxide nanoparticle concentration on the linearity and diagnostic accuracy of off-resonance imaging, NMR Biomed. 21 (2008) 453–463, http://dx.doi.org/10.1002/nbm.1209.
[37] G. Korosoglou, R.G. Weiss, D.A. Kedziorek, P. Walczak, W.D. Gilson, M. Schär, D.E. Sosnovik, D.L. Kraitchman, R.C. Boston, J.W. Bulte, R. Weissleder, M. Stuber, Noninvasive detection of macrophage-rich atherosclerotic plaque in hyperlipidemic rabbits using "positive contrast" magnetic resonance imaging, J. Am. Coll. Cardiol. 52 (2008) 483–491, http://dx.doi.org/10.1016/j.jacc.2008.03.063.
[38] S. Delangre, Q.L. Vuong, D. Henrard, J. Magat, C. Po, B. Gallez, Y. Gossuin, Theoretical and experimental study of ON-resonance saturation, an MRI sequence for positive contrast with superparamagnetic nanoparticles, J. Magn. Reson. (2015), http://dx.doi.org/10.1016/j.jmr.2015.01.007.
[39] J.-H. Seppenwoolde, M.A. Viergever, C.J.G. Bakker, Passive tracking exploiting local signal conservation: the white marker phenomenon, Magn. Reson. Med. 50 (2003) 784–790, http://dx.doi.org/10.1002/mrm.10574.
[40] J.-H. Seppenwoolde, K.L. Vincken, C.J.G. Bakker, White-marker imaging—separating magnetic susceptibility effects from partial volume effects, Magn. Reson. Med. 58 (2007) 605–609, http://dx.doi.org/10.1002/mrm.21304.
[41] V. Mani, K.C. Briley-Saebo, V.V. Itskovich, D.D. Samber, Z.A. Fayad, Gradient echo acquisition for superparamagnetic particles with positive contrast (GRASP): sequence characterization in membrane and glass superparamagnetic iron oxide phantoms at 1.5 T and 3 T, Magn. Reson. Med. 55 (2006) 126–135, http://dx.doi.org/10.1002/mrm.20739.
[42] K.C. Briley-Saebo, Y.S. Cho, P.X. Shaw, S.K. Ryu, V. Mani, S. Dickson, E. Izadmehr, S. Green, Z.A. Fayad, S. Tsimikas, Targeted iron oxide particles for in vivo magnetic resonance detection of atherosclerotic lesions with antibodies directed to oxidation-specific epitopes, J. Am. Coll. Cardiol. 57 (2011) 337–347, http://dx.doi.org/10.1016/j.jacc.2010.09.023.
[43] P.R. Seevinck, H. de Leeuw, C. Bos, C.J.G. Bakker, Highly localized positive contrast of small paramagnetic objects using 3D center-out radial sampling with off-resonance reception, Magn. Reson. Med. 65 (2011) 146–156, http://dx.doi.org/10.1002/mrm.22594.
[44] Q. Zhao, J. Langley, S. Lee, W. Liu, Positive contrast technique for the detection and quantification of superparamagnetic iron oxide nanoparticles in MRI, NMR Biomed. 24 (2011) 464–472, http://dx.doi.org/10.1002/nbm.1608.
[45] H. Zhu, K. Demachi, M. Sekino, Phase gradient imaging for positive contrast generation to superparamagnetic iron oxide nanoparticle-labeled targets in magnetic resonance imaging, Magn. Reson. Imaging 29 (2011) 891–898, http://dx.doi.org/10.1016/j.mri.2011.04.011.
[46] F. Eibofner, G. Steidle, R. Kehlbach, R. Bantleon, F. Schick, Positive contrast imaging of iron oxide nanoparticles with susceptibility-weighted imaging, Magn. Reson. Med. 64 (2010) 1027–1038.
[47] H. de Leeuw, P.R. Seevinck, C.J.G. Bakker, Center-out radial sampling with off-resonant reconstruction for efficient and accurate localization of punctate and elongated paramagnetic structures, Magn. Reson. Med. 69 (2013) 1611–1622, http://dx.doi.org/10.1002/mrm.24416.
[48] L.A. Crowe, F. Ris, S. Nielles-Vallespin, P. Speier, S. Masson, M. Armanet, P. Morel, C. Toso, D. Bosco, T. Berney, J.-P. Vallee, A novel method for quantitative monitoring of transplanted islets of langerhans by positive contrast magnetic resonance imaging: 3D radial UTE MRI for iron oxide labeled islet cells, Am. J. Transplant. 11 (2011) 1158–1168, http://dx.doi.org/10.1111/j.1600-6143.2011.03559.x.
[49] X. Deligianni, D. Jirák, Z. Berková, M. Hájek, K. Scheffler, O. Bieri, In vivo visualization of cells labeled with superparamagnetic iron oxides by a sub-millisecond gradient echo sequence, Magma 27 (2014) 329–337, http://dx.doi.org/10.1007/s10334-013-0422-3.

[50] P. Krämer, X. Helluy, T. Kampf, E. Lang, P.M. Jakob, Flow-enhanced off-resonance saturation for remote detection of iron-based contrast agents, Magn. Reson. Med. Off. J. Soc. Magn. Reson. Med. Soc. Magn. Reson. Med. 63 (2010) 1708–1715, http://dx.doi.org/10.1002/mrm.22354.
[51] C. Khemtong, C.W. Kessinger, J. Ren, E.A. Bey, S.-G. Yang, J.S. Guthi, D.A. Boothman, A.D. Sherry, J. Gao, In vivo off-resonance saturation magnetic resonance imaging of v 3-targeted superparamagnetic nanoparticles, Cancer Res. 69 (2009) 1651–1658, http://dx.doi.org/10.1158/0008-5472.CAN-08-3231.
[52] O. Zurkiya, X. Hu, Off-resonance saturation as a means of generating contrast with superparamagnetic nanoparticles, Magn. Reson. Med. 56 (2006) 726–732, http://dx.doi.org/10.1002/mrm.21024.
[53] C. Khemtong, O. Togao, J. Ren, C.W. Kessinger, M. Takahashi, A.D. Sherry, J. Gao, Off-resonance saturation MRI of superparamagnetic nanoprobes: theoretical models and experimental validations, J. Magn. Reson. San Diego Calif. 1997 (209) (2011) 53–60, http://dx.doi.org/10.1016/j.jmr.2010.12.013.
[54] Z.-P. Liang, P.C. Lauterbur, Principles of Magnetic Resonance Imaging: A Signal Processing Perspective, SPIE Optical Engineering Press, IEEE Press, Bellingham, Wash, New York, 2000.
[55] F. Bloch, Nuclear Induction, Phys. Rev. 70 (1946) 460–474, http://dx.doi.org/10.1103/PhysRev. 70.460.
[56] R. Brown, Distribution of fields from randomly placed dipoles: free-precession signal decay as result of magnetic grains, Phys. Rev. 121 (1961) 1379–1382, http://dx.doi.org/10.1103/PhysRev. 121.1379.
[57] A. Oppelt, R. Graumann, H. BarfuB, H. Fischer, W. Hartl, W. Schajor, FISP-a new fast MRI sequence, Electromedica 54 (1986) 15–18.
[58] Y. Zur, S. Stokar, P. Bendel, An analysis of fast imaging sequences with steady-state transverse magnetization refocusing, Magn. Reson. Med. 6 (1988) 175–193, http://dx.doi.org/10.1002/mrm.1910060206.
[59] K. Scheffler, A pictorial description of steady-states in rapid magnetic resonance imaging, Concepts Magn. Reson. 11 (1999) 291–304.
[60] E.M. Haacke, R.W. Brown, M.R. Thompson, R. Venkatesan, Magnetic Resonance Imaging: Physical Principles and Sequence Design, first ed., Wiley-Liss, New York, 1999.
[61] C. Westbrook, C.K. Roth, J. Talbot, MRI in Practice, Wiley-Blackwell, Chichester, West Sussex, Malden, MA, 2011. <http://www.novanet.eblib.com/EBLWeb/patron/?target=patron&extendedid=P_693813_0> (accessed 05.05.14).
[62] Q.L. Vuong, Y. Gossuin, P. Gillis, S. Delangre, New simulation approach using classical formalism to water nuclear magnetic relaxation dispersions in presence of superparamagnetic particles used as MRI contrast agents, J. Chem. Phys. 137 (2012), http://dx.doi.org/10.1063/1.4751442.
[63] P. Gillis, F. Moiny, R.A. Brooks, On T_2-shortening by strongly magnetized spheres: a partial refocusing model, Magn. Reson. Med. 47 (2002) 257–263, http://dx.doi.org/10.1002/mrm.10059.
[64] Q.L. Vuong, P. Gillis, Y. Gossuin, Monte Carlo simulation and theory of proton NMR transverse relaxation induced by aggregation of magnetic particles used as MRI contrast agents, J. Magn. Reson. 212 (2011) 139–148, http://dx.doi.org/10.1016/j.jmr.2011.06.024.
[65] D.C. Montgomery, G.C. Runger, Applied Statistics and Probability for Engineers, Wiley, Hoboken, NJ, 2011.